applied sciences

MDPI

Article

The Use of Slag, Biochar, and Hydrochar as Potential Concrete Additives: Effects on Compressive Strength and Spalling Resistance Before and After Fire Exposure

Asaad Almssad [1,*], Majid Al-Gburi [2], A. Viktor [1] and Awaz Mohammadullah [1]

[1] Department of Engineering and Chemical Sciences, Karlstad University, 651 88 Karlstad, Sweden
[2] Building and Construction Techniques Engineering, Technical Engineering College–Mosul, Northern Technical University, Mosul 41001, Iraq; majid.algburi@ntu.edu.iq
* Correspondence: asaad.almssad@kau.se

Abstract

Cement production is a significant global source of CO_2 emissions, leading to a demand for sustainable concrete alternatives. This study investigates the use of various additives to partially replace cement and assesses their effects on compressive strength and fire resistance, particularly spalling. Seven concrete mixes were tested for their initial and post-fire compressive strength, mass loss, and cracking. The cement-only reference mix (R1) achieved the highest initial strength (53.3 MPa) but experienced severe explosive spalling. In contrast, the mix with slag and polypropylene (PP) fibers (R4) offered the best balance, maintaining substantial strength after fire while completely preventing spalling. Biochar additions consistently lowered strength and increased spalling risk, whereas hydrochar notably enhanced spalling resistance, especially at higher replacement levels. The results demonstrate that sustainable additives, such as slag with PP fibers or high-dose hydrochar, can effectively improve fire safety and reduce cement use, though there is an initial trade-off in mechanical performance. Ultimately, choosing the optimal mix depends on whether environmental benefits, fire resistance, or structural strength is the highest priority.

Keywords: concrete additives; fire resistance and spalling; slag and biochar

Academic Editor: Jason G. Parsons

Received: 27 October 2025
Revised: 4 December 2025
Accepted: 8 December 2025
Published: 18 December 2025

Citation: Almssad, A.; Al-Gburi, M.; Viktor, A.; Mohammadullah, A. The Use of Slag, Biochar, and Hydrochar as Potential Concrete Additives: Effects on Compressive Strength and Spalling Resistance Before and After Fire Exposure. *Appl. Sci.* **2025**, *15*, 13248. https://doi.org/10.3390/app152413248

1. Introduction

Concrete is the most widely used construction material worldwide because it combines structural reliability with cost efficiency [1]. However, its environmental impact, especially regarding climate change, is mainly driven by the cement binder: process emissions from limestone calcination and high-temperature kiln operations account for about 7–9% of global CO_2 emissions. Sweden's legally grounded climate framework aims for net-zero greenhouse gas emissions by 2045, highlighting the importance of reducing clinker content and increasing the use of alternative binders in practice. In the concrete industry's full lifecycle, cement typically accounts for the largest share of embodied carbon, underscoring the potential for decarbonization through clinker substitution [2].

Supplementary cementitious materials (SCMs), such as ground-granulated blast furnace slag (GGBS) and coal fly ash, are established methods to lower embodied emissions while maintaining performance [3]. However, their availability is limited as the steel industry decarbonizes and coal-fired power plants shut down, prompting research into alternative precursors such as calcined clays and natural pozzolans, as well as biogenic carbon-based fillers. Biochar (produced via pyrolysis) and hydrochar (produced

via hydrothermal carbonization) are particularly interesting for enhancing circularity and potentially altering pore structure and hydration behavior at low replacement levels. Additionally, polypropylene (PP) microfibers are often studied to prevent fire-induced explosive spalling by increasing temporary permeability and relieving vapor pressure during high temperatures [4].

While much research has focused on mechanical strength and environmental impact, the fire behavior of alternative fillers remains less understood [5]. Spalling, in which surface layers of concrete violently detach during fire, poses serious safety risks, especially in load-bearing structures [6]. Therefore, the fire performance of new additives must be carefully evaluated to verify their suitability for structural use [7].

This study addresses a dual challenge at the heart of sustainable structural engineering: lowering clinker content in concrete to achieve Sweden's net-zero 2045 target while maintaining reliable performance under fire conditions. Although polypropylene (PP) microfibers are commonly used to prevent explosive spalling by increasing permeability at high temperatures, their combined effects with biogenic fillers such as biochar (from pyrolysis) and hydrochar (from hydrothermal carbonization) in low-cement mixes are not yet fully understood [8]. This knowledge gap drives a thorough examination of how these additives affect mass loss, crack formation, and residual strength after heating [9]. Therefore, the study focuses on three related questions: which formulation provides the highest compressive strength before and after fire exposure; how biochar, hydrochar, and PP fibers influence spalling tendency and mass loss; and what relationships exist between crack patterns and the type and amount of additives used [10].

The goal is to produce decision-relevant evidence for climate-conscious mix design by systematically comparing two conventional controls with five experimental formulations that vary the proportions of biochar, hydrochar, and PP fibers. Using standardized pre- and post-heating testing, the analysis measures changes in compressive strength, mass loss, and visually assessed damage, enabling a comparative assessment of thermomechanical robustness [11]. The main aim is to clarify additive–response relationships (strength retention, spalling behavior, cracking modes) to guide the practical specification of lower-cement concretes without compromising safety margins under fire conditions. The scope is intentionally limited to isolate material effects, including unreinforced specimens, no chemical admixtures beyond the defined fillers, no measurement of moisture content, and no external mechanical loading during heating. Fire tests are viewed as a comparative materials study rather than a formal reaction-to-fire classification under EN 13501-1 [12]; the standard is only referenced to provide context for classification concepts, not to claim a product rating. These choices enhance internal validity but restrict direct application to reinforced members, service moisture states, and load-bearing, restraint-sensitive boundary conditions; such cases require specific follow-up testing under the appropriate standards and conditions.

Mechanisms and Mitigation of Fire-Induced Spalling

Spalling is a critical deterioration phenomenon in fire-exposed concrete, characterized by the rapid or progressive detachment of material layers under thermal loading [13]. Its occurrence is closely linked to unfavorable hygrothermal conditions, exceptionally high internal moisture, low permeability, fragile pore structures, and high heating rates exceedingly approximately 3 °C/min. These factors interact to increase the risk of sudden material loss and structural weakness. Mechanistically, spalling results from three interconnected processes: (i) pore-pressure buildup within the vaporization front, (ii) thermal strain gradients between the heated surface and the cooler interior, and (iii) the gradual loss of tensile strength in the heated matrix [13]. The depth profile of fire-exposed concrete

can be simplified into three distinct zones (Figure 1). At the surface, the dry zone is free of free water due to high temperatures. Beneath this, the vaporization zone develops, where liquid water evaporates and internal pore pressures reach their peak. The saturated zone represents the cooler, moisture-rich core of the specimen. When vapor pressures in the vaporization zone surpass the tensile strength of the surrounding matrix, explosive spalling may occur, usually within the first 10–30 min of fire exposure. This results in a reduction in effective cross-section, early reinforcement exposure, and significant loss of fire resistance [14].

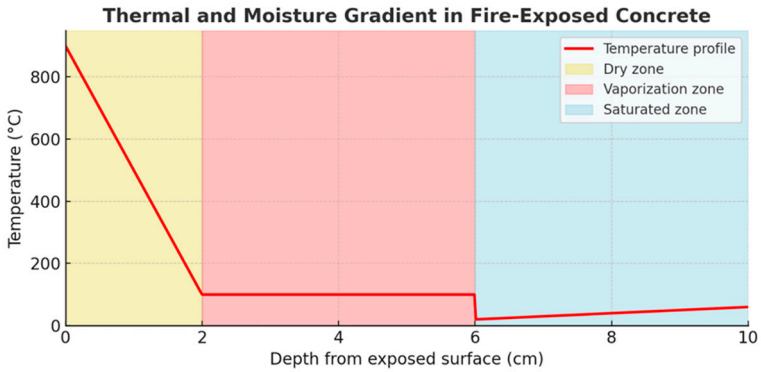

Figure 1. Idealized hygrothermal profile in fire-exposed concrete [12].

Mitigation strategies aim to reduce the probability and severity of spalling. A common approach is to control the initial moisture content (e.g., maintaining ~3% at testing or commissioning). Polypropylene (PP) fibers, melting at ~165 °C, are often added to create transient venting channels that relieve pore pressure. Additionally, the use of lightweight or pervious aggregates can increase permeability and reduce vapor build-up. EN1992-1-2 recommends performance-based verification, supported by laboratory heating testing, to calibrate detailing rules and cover thicknesses [15]. In practice, project specifications typically define acceptable spalling depths (e.g., ~10 mm average, up to ~40 mm maximum), ensuring structural safety under standardized furnace conditions.

2. Materials and Methods

Concrete is a multiphase composite composed of a hydraulic binder (typically Portland cement), water, and graded mineral aggregates [16]. Based on the cement used in structural concrete, it usually contains at least 95% clinker by mass. This clinker is produced by calcining limestone ($CaCO_3$) and clay at approximately 1450 °C; during final grinding, a small, controlled amount of calcium sulfate (gypsum/anhydrite) is added to regulate setting and prevent flash set [17]. When it contacts water, exothermic hydration reactions produce calcium-silicate-hydrate (C–S–H), the main binding phase responsible for strength and cohesion, along with portlandite and other hydrates [18]. Aggregates, often quartz-rich sands, gravels, or crushed rock, are proportioned into complementary size ranges (e.g., 0–8 mm and 8–16 mm) to maximize packing density, reduce interparticle voids, and thereby lower paste demand while improving dimensional stability [19]. The water-to-cement mass ratio (w/c) is the key mixture parameter affecting microstructure, porosity, transport properties, and strength. Lower w/c ratios (around 0.30–0.40) produce a denser, more durable matrix with higher compressive strength but lower workability. Rheology at low water-to-cement ratios is typically restored using high-range water-reducing admixtures (superplasticizers), which disperse cement particles without adding free water [20].

Despite its usefulness, traditional cement-based concrete has a significant environmental impact. The cement industry produces about 7–9% of global human-caused CO_2 emissions [21]. Around 60% of these emissions come from chemical processes, mainly the

decarbonation of limestone during clinker production, while the remaining approximately 40% result from fuel burning to maintain kiln temperatures [22]. Additionally, indirect (Scope 2) emissions from electricity use, including grinding and auxiliary operations, add to the overall footprint. Overall, the evidence shows that both process-related and energy-related sources need to be addressed together [23]. In Europe, the concrete supply chain is estimated to emit about 150 million tons of CO_2 equivalent annually, which accounts for roughly 8% of emissions from the construction sector [24]. While different countries have varying paths based on fuel choices, clinker levels, and construction activity, sector data indicates consistent progress through the use of alternative fuels and clinker replacement. Notably, recent EU data shows an average of over 50% thermal substitution with non-recyclable waste and biomass. However, these improvements alone are not enough to meet net-zero goals without faster action across design, materials, and manufacturing processes [21].

To reduce embodied carbon, standards and industry roadmaps exemplified by EN 206:2020 promote a set of strategies [25]. First, replacing clinker with supplementary cementitious materials (SCMs) lowers process emissions and can improve durability; common options include GGBFS, fly ash, natural pozzolans, calcined clays, and limestone additions, as well as LC^3-type blends meeting performance standards [26]. Second, moving to low-carbon energy through increased thermal substitution, selective electrification, and renewable energy procurement cuts combustion-related emissions; EU plants already show high substitution rates with room for further improvement [27]. Third, carbon capture, utilization, and storage (CCUS) are essential for the hardest-to-decarbonize process segments; early commercial deployment at Heidelberg Materials' Brevik plant demonstrates post-combustion capture combined with permanent storage and market-ready net-zero cement products [28]. Lastly, enhanced natural carbonation—both during service and at end-of-life—through optimized exposure and concrete recycling can significantly reabsorb CO_2 over decades, now recognized in international assessments and accounting standards [29]. Together, these measures, strengthened by performance-based specifications, low-carbon procurement, and EPDs, offer a credible path to substantially lowering life-cycle impacts while maintaining structural performance.

2.1. Mechanical Behavior and Compressive Strength

2.1.1. Strength Mechanisms

Concrete's compressive strength, fc, the main design parameter in structural uses, measures the material's ability to resist axial compressive loads and is essential for member sizing, detailing, and safety checks; when measured on standard cylinders or cubes, fc reflects the combined effects of mixture design and curing [30]. At the microscale, the mechanical performance of cementitious systems depends on total and connected porosity, pore-size distribution, and the continuity of the hydrate network. These factors are mainly influenced by the water-to-cement ratio (w/c), the degree of hydration, and the curing process. Under standard curing conditions (20 ± 2 °C and $\geq$95% relative humidity), hydration occurs steadily, reducing capillary porosity and increasing gel space utilization. Conversely, insufficient moisture or suboptimal temperature conditions slow hydration, maintaining a percolated capillary pore system and resulting in a weaker hardened matrix [31,32].

During hydration, clinker phases form a binding matrix mainly made of calcium-silicate-hydrate (C–S–H), with portlandite and other hydrates forming simultaneously [33]. The volume, shape, and packing of these hydrates determine the stiffness and fracture resistance of the paste [34]. Cement fineness speeds up early hydration by increasing surface area and nucleation sites, improving early-age strength but potentially raising the risks of heat release and autogenous shrinkage if not properly managed through mixture

design and curing [35]. At the mesoscale, aggregate properties influence strength through packing and mechanical restraint: well-graded aggregates reduce paste demand and lower interparticle voids, while aggregate stiffness, surface texture, and mineralogy affect stress transfer and the properties of the interfacial transition zone (ITZ) [29]. A denser ITZ limits microcrack initiation and growth under load, which delays localization and increases the measured fc [36].

2.1.2. Testing Protocols

Compressive strength is determined in accordance with EN 12390-3 [37] for method and result expression, with specimen geometry and tolerances specified in EN 12390-1 [38], specimen manufacture and curing in EN 12390-2 [39], and machine performance in EN 12390-4 [40]. Standard specimens are 150 × 150 × 150 mm cubes or 150 × 300 mm cylinders. The test age is typically 28 days unless otherwise specified by the standard [41]. Before testing, bearing faces are prepared (mould-cast for cubes; ground or capped for cylinders), and specimens are centered within 1% of the designated size or diameter. Packing elements other than auxiliary platens or spacing blocks are not permitted. Loading is applied without shock at a constant rate of 0.6 ± 0.2 MPa s^{-1} after a brief initial load (~≤30% of the expected failure load). The maximum load is recorded, and the compressive strength is expressed to the nearest 0.1 MPa. Testing machines must meet the force-measurement accuracy, platen stiffness/parallelism, and control requirements of EN 12390-4 [40]. The result is calculated using Equation (1), with the designated cross-sectional area (EN 12390-1) or measured dimensions where necessary applies:

$$f_c = \frac{P_u}{A} \quad (1)$$

where Pu is the peak load (N) and A is the loaded area (mm^2). When cylinders are tested, projects that report cube-equivalent strengths shall apply the documented conversion relationships (e.g., Eurocode/EN 206 context) rather than a single generic factor; in normal-strength ranges, the characteristic cylinder strength is commonly ≈80% of the cube value, but national annexes and calibrated datasets should govern the correlation used. The typical progression of failure modes is illustrated in Figure 2a,b. Note: the constant loading rate of 0.5 MPa/s used in this study lies within the EN 12390-3 prescribed range (0.6 ± 0.2 MPa/s).

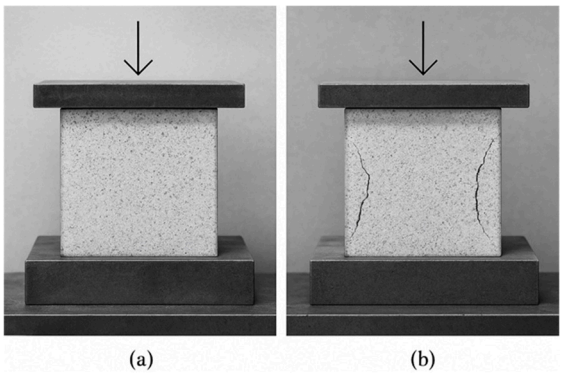

Figure 2. Concrete compressive strength failure mechanism: (**a**) elastic loading; (**b**) cracking at peak load.

2.2. Supplementary and Alternative Fillers

Ground-Granulated Blast-Furnace Slag (GGBFS)

GGBFS, an ironmaking by-product, is a latent-hydraulic glassy material rich in CaO–SiO_2–Al_2O_3–MgO (see Figure 3). In the high-alkalinity pore solution of cementitious

systems, it hydrates slowly, generating secondary C–S–H that refines pore structure and densifies the matrix [42]. Partial replacement of Portland cement with GGBFS in the 35–65% range typically reduces the heat of hydration, improves resistance to chloride ingress and sulfate attack, and enhances long-term durability [43]. Early-age strength may be lower relative to neat Portland systems, but strength development beyond 28 days is usually comparable or superior when adequate curing conditions are present [44,45].

Figure 3. SEM images of Ground-granulated blast-furnace slag (GGBFS).

Polypropylene Fibers

Polypropylene (PP) fibers (Figure 4), as defined in ACI 544.4R-18, are used to improve ductility and mitigate fire-induced spalling [46]. The polypropylene fibers used in this study had the following specifications:

Figure 4. Polypropylene fibers are distributed in the concrete matrix.

Nominal length: 12 mm, diameter: 18 μm (micrometers), aspect ratio: ≈667. Their melting near ~165 °C creates transient vapor-relief pathways that limit pore pressure buildup at elevated temperatures. At ambient conditions, micro-PP fibers have a limited effect on compressive strength, but they reduce plastic shrinkage cracking and enhance post-crack energy absorption; effectiveness under fire exposure depends on fiber dosage, geometry, and dispersion [47].

Biochar

Biochar is a porous, carbonaceous material produced via biomass pyrolysis (~500–700 °C) (see Figure 5). Its high surface area and sorptivity can promote internal curing and reduce autogenous and drying shrinkage; however, depending on the feedstock, activation, and dosage, biochar may reduce early-age compressive strength. Typical experimental dosages range from 0.5% to 2% by mass of binder. Careful surface treatment, grading, and mix optimization are recommended to manage workability and air-entrainment effects [48–50].

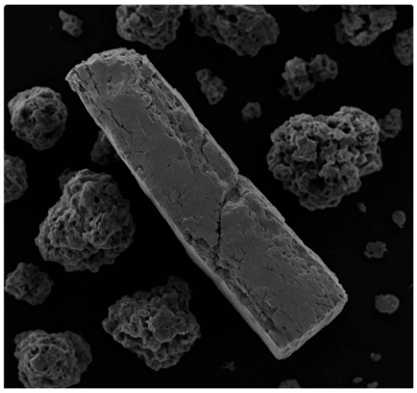

Figure 5. SEM image of porous biochar particles.

Hydrochar

Hydrochar, produced by hydrothermal carbonization (≈200–250 °C), contains more oxygenated (acidic) functional groups and exhibits lower carbon crystallinity than biochar (see Figure 6). These chemical features distinguish its effects on rheology, setting, and early hydration, often necessitating lower dosages or surface modification to achieve balanced fresh-state and strength performance [51].

Figure 6. Hydrochar granules before grinding.

2.3. Standardized Testing and Building Regulations

Fire performance of concrete members is assessed under standardized furnace exposures that approximate severe compartment fires [52]. Internationally, ISO 834-1 and ASTM E119 are the primary test standards; European structural design under fire follows EN 1992-1-2 (Eurocode 2: Structural Fire Design for Concrete) [53]. ISO 834-1 specifies the nominal time–temperature (cellulosic) curve:

$$\theta_g(t) = 20 + 345log_{10}(8t + 1) \quad (2)$$

where θg is the furnace temperature (°C) and t is time (min). This curve rises rapidly to ≈680 °C at 10 min, reaches ≈840–950 °C by 30–60 min, and exceeds ~1000 °C by ~90 min, representing post-flashover conditions [54]. Figure 7 illustrates the ISO 834-1 curve used for regulatory testing of structural elements.

For specific building components, EN 1365-1 defines the fire-resistance test for load-bearing walls, while EN 1992-1-2 provides design rules (tabulated methods, simplified/advanced calculations) [55], for reinforced and prestressed concrete under fire. In Sweden, Boverket's Building Regulations (BBR 31) incorporate these European standards within national provisions, complemented by guidance on sustainability and safety [56].

Together, this framework enables consistent furnace testing, performance classification, and structural fire design.

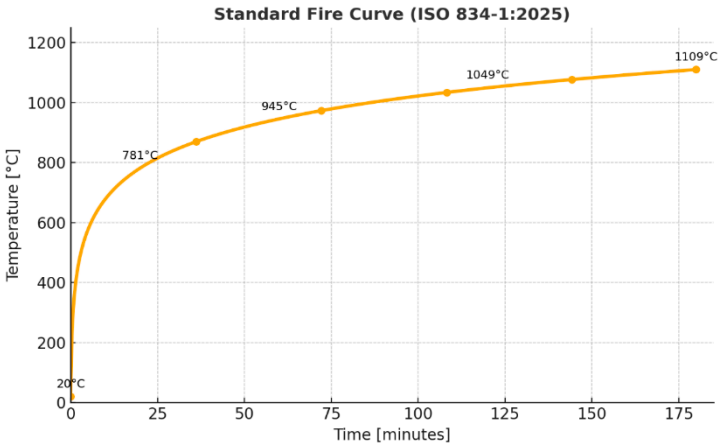

Figure 7. Standard fire curve used for regulatory heating testing of structural elements [53].

2.4. Thermal Degradation and Stages of Fire Exposure

Concrete response under fire is governed by the coupled action of thermal and mechanical stresses arising from steep temperature gradients. In enclosed compartments, fire development typically proceeds through four phases: ignition, growth to flashover, fully developed fire, and decay, as illustrated in Figure 8 [57]. Each phase imposes distinct thermo-mechanical demands on the material. During ignition and growth, surface temperatures rise progressively, causing differential expansion between the paste and aggregate and initiating microcracking near the heated face [58,59]. At flashover (~600 °C), near-simultaneous ignition of fuels triggers a rapid temperature escalation; pore pressure rises as free and bound water vaporize, intensifying microcrack formation [60]. In the fully developed phase (often approaching ~1000 °C), thermal gradients and restrained dilation promote crack coalescence; the C–S–H gel progressively decalcifies and portlandite decomposes, degrading stiffness and strength [61]. Dense, low-permeability concretes are especially susceptible because reduced venting accentuates internal pressures and thermal stresses. The decay phase lowers temperatures, but damage accumulated in earlier stages governs residual capacity [62].

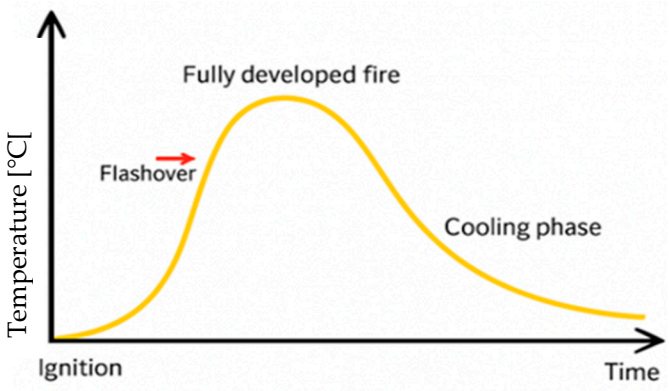

Figure 8. The four phases of compartment fire development: ignition, flashover, fully developed, and decay, (ISO/TR 17225:2002) [53].

Each phase presents specific thermo-mechanical challenges. During ignition and growth, surface temperatures increase gradually [63]. At flashover (~600 °C), near-simultaneous ignition of combustibles causes a rapid temperature rise, leading to microcracking and pore

pressure buildup. The fully developed stage reaches temperatures up to 1000 °C, which weakens the C–S–H matrix and degrades portlandite [64]. Thermal gradients create internal stresses, especially in high-strength or dense concretes with low permeability.

2.5. Post-Fire Residual Strength Testing

Half of the fire-exposed specimens were tested in compression using the same setup described in Section 7.4. Before loading, the bearing surfaces were lightly cleaned to remove loose residues that could interfere with platen contact. The cubes were then allowed to reach ambient temperature to prevent thermal gradient effects during testing. This process allowed for a direct assessment of residual strength and damage patterns based on mix design and additive content, connecting observed crack networks and mass loss to retained load-bearing capacity.

2.6. Methodological Validity and Limitations

The experimental framework adhered to international norms SS-EN 12390 and ISO 834-1, providing a strong foundation for reproducibility and external comparison. Strengths of the approach included systematic compliance with these standards, consistent environmental control during mixing, curing, heating, cooling, and testing, as well as using multiple specimens (n = 3) per recipe to improve statistical reliability. However, several limitations were recognized. Internal stress and temperature fields could not be reconstructed because embedded strain or temperature sensors were not used; furnace exposure was carried out without sustained structural loading, which limits direct application to load-bearing members in service; and spalling severity was estimated from mass loss rather than measured through depth profiling, which may underestimate localized damage at edges and corners. These limitations were addressed through careful protocol standardization and transparent reporting of all boundary conditions [65].

2.7. Method

The experimental program evaluated the fire resistance and post-fire mechanical performance of concretes incorporating environmentally sustainable constituents [66]. Mixes were modified with ground-granulated blast-furnace slag (GGBFS), biochar, and hydrochar and assessed for both thermal response and residual strength. Methodological rigor, transparency, and replicability were prioritized. All procedures followed harmonized European standards, principally the SS-EN 12390 series for mechanical testing and ISO 834-1 for furnace exposure, so that outcomes are directly comparable with contemporary research on high-performance, fire-resilient cement-based composites. Where relevant, constituent quality and production requirements adhered to EN 206:2020 and cement specifications [67].

3. Materials and Mix Proportions

Seven different concrete combinations were created: six modified mixes (R2–R7) with varying amounts of GGBFS, biochar, hydro-char, and polypropylene (PP) fibers, and one control mix (R1) made with CEM I 42.5 N. For each mix design, three identical specimens were prepared to ensure statistical reliability and account for experimental variability. The mean values obtained from these triplicate measurements are used in all test findings given in this study. Based on proven methods for lowering embodied carbon and improving concrete's fire performance, the material replacements were chosen. Each concrete mix was cast into three identical cubes. The results are presented as the mean ± 2 MPa, standard deviation. All materials were selected for their relevance to sustainable construction practices and verified to comply with the requirements of [6,12].

3.1. Material Properties

All samples were oven-dried at 105 °C to standardize moisture content before batching. Helium pycnometry was used to determine the actual particle densities for input into mixture design and porosity estimates:

- CEM I 42.5 N: ρ (density) = 3100 kg m^{-3}.
- Siliceous sand (0–8 mm) and crushed gravel (8–16 mm): ρ = 2650 kg m^{-3}.
- Biochar and hydrochar: ground to a fine powder with median particle size $D_{50} \approx 75$ µm.

Mixing water met the quality criteria of EN 206:2020. PP fibers used in R4 had a nominal length of 12 mm and a diameter of 18 µm, which were selected to enhance thermal stability and reduce the risk of explosive spalling under standard fire exposure conditions.

3.2. Reference Concrete Composition

The control mixture (R1) was proportioned to comply with the requirements of strength class C35/45 as specified in EN 206. Aggregate grading was selected in accordance with standardized sieve distribution curves to achieve dense packing and minimize void content, thereby enhancing both strength potential and durability. The total binder content was adjusted to balance mechanical performance and fresh-state workability, in accordance with conventional mix design methodologies. The complete mix proportions, along with the measured fresh-state properties, are summarized in Table 1. This control mixture served as the reference baseline against which the effects of incorporating supplementary cementitious materials, including ground granulated blast-furnace slag (GGBFS), biochar, hydrochar, and polypropylene (PP) fibers, were systematically evaluated in mixtures R2–R7 [68].

Table 1. Composition of Reference Concrete Mix.

Constituent (kg/m^3)	Symbol	Target Dose	Tolerance (±%)	Dry Mass Fraction (%) ‡
CEM I 42.5 N	c	350	2	19.3
Siliceous sand (0–8 mm)	f	670	2	36.9
Crushed gravel (8–16 mm)	g	1230	2	67.8
Mixing water	w	140	2	—

‡ Normalized to the total dry solids to align with environmental life cycle assessment (LCA) procedures.

3.3. Modified Mix Designs

Cement replacement was carried out based on the total volume to maintain mix rheology. GGBFS was added at 50% in R2 and R4, while biochar (R3) and hydrochar (R5–R7) were included at increasing doses up to 20% to assess performance limits. Table 2 shows the dosages for all materials.

Table 2. Mix Designs with Cement Replacements and Additives.

Mix ID	Cement (kg)	Slag (kg)	Biochar (kg)	Hydrochar (kg)	PP Fibre (kg)	w/b Ratio
R1	2.40	—	—	—	—	0.48
R2	1.20	1.20	—	—	—	0.60
R3	2.16	—	0.24	—	—	0.48
R4	1.20	1.20	—	—	0.010	0.60
R5	2.28	—	—	0.12	—	0.48

Table 2. *Cont.*

Mix ID	Cement (kg)	Slag (kg)	Biochar (kg)	Hydrochar (kg)	PP Fibre (kg)	w/b Ratio
R6	2.16	—	—	0.24	—	0.48
R7	1.92	—	—	0.48	—	0.48

Each mix also included 12.84 kg of aggregate and 1.14 L of water per 150 mm cube. Weighing was conducted using calibrated F1-class precision balances with an accuracy of ±0.1 g.

4. Specimen Fabrication and Curing

4.1. Molding and Mixing Process

Steel cube molds conforming to SS-EN 12390-1 [38] were cleaned, assembled to the specified tolerances, and lightly coated on the internal faces with a PTFE (polytetrafluoroethylene) release agent. Mixing was performed in a 120 L forced-action pan mixer (see Figure 9). The batching sequence followed a dry-to-wet protocol to promote uniform dispersion: (i) charge and pre-blend the dry aggregates, (ii) add the cementitious binders and mix to a consistent dry blend, and (iii) introduce the mixing water progressively while the mixer runs to prevent agglomeration and ensure homogeneous wetting. Between batches, the mixer and tools were cleaned of residue to prevent cross-contamination. The resulting fresh concrete was then immediately used for casting and subsequent curing, as specified in the test plan.

Figure 9. Forced-action mixer employed for homogenizing all concrete batches.

4.2. Casting and Compaction Technique

Fresh concrete was poured into molds in two equal layers. Each layer was compacted for 20 s using a calibrated vibrating table to eliminate entrapped air and ensure uniform density (Figure 10). Manual rodding was excluded to prevent fiber clumping and segregation.

4.3. Moisture Retention and Curing Protocol

Immediately after casting, all specimens were tightly wrapped in polyethylene film to prevent early evaporation, minimize plastic shrinkage, and reduce initial surface carbonation [69]. The molds were placed on vibration-isolated wooden pallets, ensuring the setting proceeded without disturbance and reducing the risk of microcrack initiation as the paste transitioned from a plastic to a rigid state. After 24 h, once handling strength had developed, the specimens were demolded and transferred directly to a lime-saturated water bath

maintained at 20 ± 1 °C [70]. The saturated, alkaline environment maintains equilibrium with portlandite, limits the leaching of soluble ions, and promotes the continued hydration of unreacted clinker phases; the bath temperature was monitored to ensure uniform curing throughout the immersion period. In view of the retarding effect of hydrochar, mixes R6 and R7 underwent an additional four days of sealed, room-temperature curing before immersion, a practice consistent with recognized curing guidance for mixtures exhibiting delayed setting and low permeability [71]. The sequence of film covering, undisturbed setting, demolding at 24 h, temperature-controlled lime-saturated curing, and a sealed pre-immersion hold for hydrochar-modified mixes standardized boundary conditions across all formulations. while acknowledging the distinct kinetics introduced by hydrocar in R6–R7.

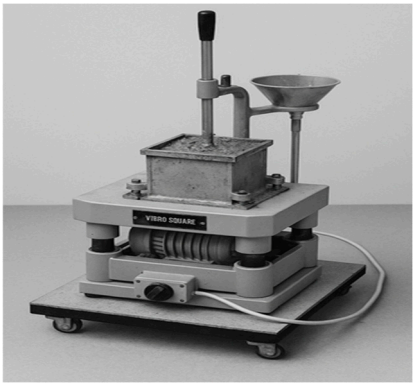

Figure 10. The compaction process utilizes a vibrating table for each layer of cubes.

5. Fire-Resistance Testing in Accordance with ISO 834-1:2025

5.1. Furnace Exposure Setup

Thermal degradation was evaluated using a radiant-heat furnace configured to simulate ISO 834-1:1:2025 conditions [65]. Each 150 mm cube was placed at the center of the refractory hearth and aligned with the viewing port to ensure symmetrical radiative and convective heating while minimizing edge effects (see Figure 11). Before each test, the chamber was preheated to stabilize the control system. Door seals and refractory linings were inspected for leaks, and reference thermocouples were verified against the set points to confirm conformity with the required profile. Specimens rested on low-conductivity ceramic spacers to prevent parasitic heat sinks and promote uniform thermal boundaries. The loading frame and metallic accessories remained outside the hot zone to avoid unintended shielding. The furnace atmosphere was maintained at a constant temperature between tests to enhance comparability across different mixtures.

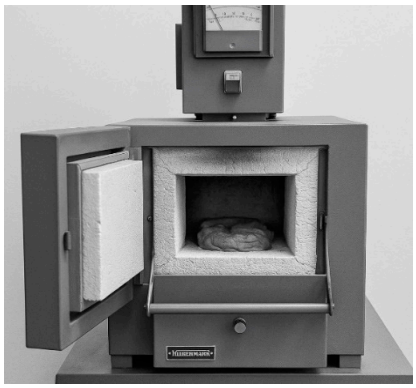

Figure 11. The high-temperature furnace is used to expose specimens under the ISO 834-1:2025 thermal conditions.

5.2. Thermal Profile and Time Intervals

According to ISO 834-1:2025, the standard fire curve depicts a logarithmic time-temperature trajectory characteristic of post-flashover compartment fires [72]. Specimens were exposed for 60 min, with the corresponding benchmark set points summarized in Table 3. Throughout the exposure, furnace control and monitoring were maintained to ensure adherence to the programmed ramp while avoiding door openings that could cause transient cooling, thereby promoting a uniform thermal field around the specimens. After heating, the specimens were allowed to cool in place until the internal temperature dropped to approximately 250 °C, a controlled procedure meant to limit quench-induced thermal shock and microcracking while allowing safe handling. This protocol ensured a consistent thermal history across all mixes, enabling a direct comparison of damage indicators and residual capacity under the ISO 834-1:2025 regime.

Table 3. ISO 834-1 Fire Exposure Schedule.

Time (min)	Temperature (°C)
15	750
30	840
60	950

6. Compressive Strength Testing

6.1. Testing Procedure and Machine Calibration

Mechanical performance was assessed through uniaxial compressive testing in accordance with the European standard EN 12390-3 [37]. Each specimen was positioned perpendicular to the casting direction and aligned concentrically within the testing frame using reference marks. Specimens were placed on clean, leveled platens to ensure uniform stress distribution during loading. Light grinding of the bearing faces was undertaken when required to restore planarity. Loading was applied continuously at a rate of 0.6 MPa/s, and the machine was verified within the laboratory's calibration schedule to ensure that force measurement accuracy, platen parallelism, and system compliance met the stated tolerances. The test environment (temperature and humidity) was kept constant to reduce variability across replicates.

6.2. Strength Calculation Formula

Immediately prior to testing, the loaded-face dimensions were measured with a calibrated gauge to capture any deviation from nominal size. Compressive strength was then computed using Equation (1) with the designated bearing area (or the measured area where applicable), and results were reported to 0.1 MPa in line with the referenced standards. Replicates for each mixture were averaged, and dispersion was monitored to confirm manufacturing consistency. Any outliers were checked against specimen records for casting or curing irregularities.

6.3. Surface Cracking and Mass Loss Assessment

6.3.1. Visual Inspection and Fracture Documentation

Failure modes were documented using high-resolution digital imaging with consistent diffuse lighting and a fixed stand-off distance [73]. The surface condition was recorded both before and after furnace exposure, and the same face was revisited, when possible, to enable direct comparison. Particular attention was given to surface cracking, delamination, and spalling, with qualitative mapping of crack density and orientation—especially for biochar- and hydrochar-modified mixes—to differentiate microcracking near the heated

face from deeper fractures traversing the core. Scale bars were included in each frame to support subsequent measurements.

6.3.2. Quantitative Mass Loss

Specimens were weighed before and after furnace exposure on a precise balance once they had equilibrated to ambient temperature. The mass change provided an indirect measure of moisture loss, matrix deterioration, and early spalling severity, following the method described by Boström [68]. To minimize weighing bias, loose surface debris was gently removed without disturbing the adherent material. Balances were zeroed before each batch, and repeat measurements were taken if readings differed by more than 0.1% of the specimen mass.

7. Results and Discussion

This section combines the experimental results for all mix designs under pre-fire and post-fire conditions. We examine how partial replacement of Portland cement with GGBFS, biochar, and hydrochar influences mechanical performance, thermal degradation, and mass stability. The presentation follows the methodological order and connects qualitative fracture evidence (crack patterns) with quantitative metrics (strength retention). To enhance understanding, the results are discussed with reference to known hydration mechanisms (e.g., clinker dissolution, latent hydraulic/pozzolanic reactions) and porosity development, while keeping reference to the figures and tables produced in this study. When relevant, we highlight expected sensitivities to curing and temperature history, variability in specimens, and microstructural factors such as the interfacial transition zone (ITZ). Overall, the analysis combines visual observations with measured strengths to offer a clear account of how each additive influences the load-bearing structure before and after thermal exposure.

7.1. Pre-Fire Compressive Strength Testing

Pre-fire compressive strength was measured according to EN 12390-3 [37]. Figure 12 and Table 4, compares the seven mixes at the test age. As expected, the control R1 (cement–aggregate–water only) achieved the highest strength (53.3 MPa), consistent with Portland-cement systems where a low water/cement ratio promotes a dense hydrate network, limited capillary porosity, and thus high load-bearing capacity. R1's performance sets a benchmark for evaluating the effects of cement substitution. In contrast, the hydrochar series showed a steady decline with increased replacement. R5 (5%), R6 (10%), and R7 (20%) registered progressively lower strengths, with R7 showing the lowest among all mixes. This trend aligns with reduced hydraulic bonding when a mostly non-hydraulic, carbon-rich filler displaces clinker: at the tested dosages, hydrochar does not provide enough pozzolanic reactivity to produce additional C–S–H, and its high specific surface area can increase water demand, worsen internal porosity, and disrupt particle packing. Any potential micro-filler benefits seem to be outweighed by the decrease in reactive cement and the resulting weakening of the percolated hydrate network. The decline also matches expectations that the nucleation/seed effects of carbonaceous particles are limited at these replacement levels and curing conditions. The GGBFS-blended R2 (50% replacement) showed about 21% lower strength than R1, reflecting the slower early hydration kinetics of slag. This behavior is typical at 28 days for mixes with significant slag content and depends on the curing regime and temperature [73]. In such systems, the latent hydraulic reactions of GGBFS need adequate alkalinity and time to significantly contribute to C–S–H formation. Before these conditions are achieved, early-age stiffness and strength may remain suppressed compared to pure Portland cement. The addition of PP fibers in R4 (with 50% GGBFS) did not offset this early-age shortfall, and its measured strength also lagged behind the control.

This finding aligns with the understanding that micro-fibers mainly influence crack control and ductility rather than increasing intrinsic compressive strength at low strains. Similarly, R3 (10% biochar) underperformed compared to R1, consistent with the expected early-age response of composite binders containing high-surface-area carbonaceous fillers that modify water distribution and pore structure without delivering comparable pozzolanic benefits within the tested timeframe. Collectively, these observations indicate that, at the examined replacement levels and curing schedule, strength development is governed by (i) the balance between reactive clinker and latent hydraulic/pozzolanic constituents, (ii) the evolution of porosity (capillary and interfacial), and (iii) the extent to which additives act as inert diluents versus reactive binders. The ranking across R1 > R2/R4/R3 > R5 > R6 > R7 mirrors this balance and provides a baseline for interpreting strength retention after thermal loading.

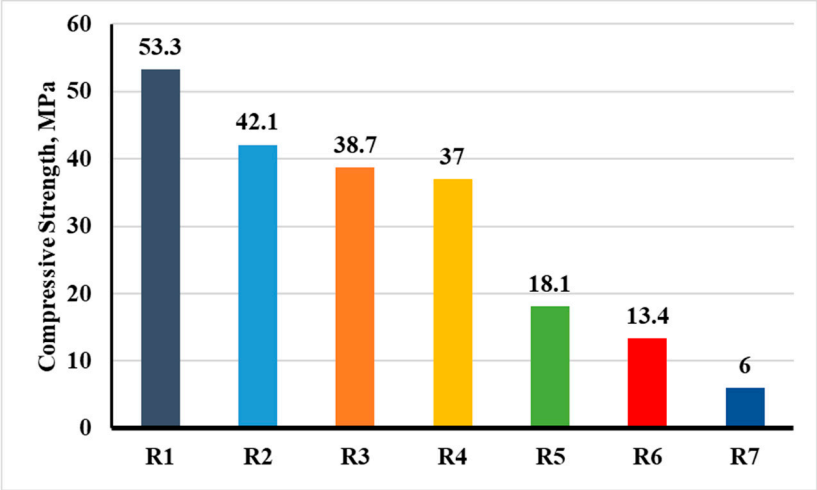

Figure 12. Variation in compressive strength for different recipes before fire exposure.

Table 4. Estimated pre-fire compressive strengths based on experimental trend.

Recipe	Cement (%)	Additive	Pre-Fire Strength (MPa)
R1	100	—	53.3 ± 2
R2	50	50% GGBFS	42.0 ± 2
R3	90	10% Biochar	39.0 ± 2
R4	50	50% GGBFS + PP fibre	37.0 ± 2
R5	95	5% Hydrochar	36.0 ± 2
R6	90	10% Hydrochar	30.0 ± 2
R7	80	20% Hydrochar	21.0 ± 2

Surface Cracking from Pre-Fire Compression

Surface cracking patterns (Figure 13a–g) provide qualitative insight into stress redistribution and matrix–aggregate interaction before thermal exposure and, by extension, into how each binder system accommodates inelasticity and microcrack growth:

- **R1 (Figure 13a):** Fine, uniformly distributed hairline cracks, characteristic of a dense matrix near the elastic–inelastic transition, where microcracking initiates but remains well constrained by a strong paste skeleton. The pattern suggests efficient stress diffusion and a relatively robust ITZ.
- **R2 (Figure 13b):** Slightly wider cracking and a detached corner fragment. Early-age slag systems can exhibit altered ITZ chemistry and lower early bond strength, leading

to localized stress intensification and more pronounced edge damage under peak load, consistent with observations for slag-blended concretes [15].

- **R3 (Figure 13c):** Fewer, more diffuse cracks, indicating elevated internal porosity and a softer matrix. While reduced stress concentration may delay coalescence, the concomitant loss of stiffness limits peak strength, matching the measured reduction relative to R1.
- **R4 (Figure 13d):** No visible surface cracking at the specimen faces. PP fibres likely bridged microcracks during loading, restricting surface expression of fracture and promoting a more distributed damage field—behaviour widely reported for fibre-reinforced concretes under compression [34].
- **R5 (Figure 13e):** No visible cracking at 5% hydrochar, consistent with a matrix still dominated by cement hydration products and with microcracks either below the surface or too fine to resolve visually at the employed documentation scale.
- **R6 (Figure 13f)**: Localized detachment of two fragments, indicative of weak interfacial bonding and early microcrack coalescence into shallow surface spalls. This suggests stress concentration at heterogeneities introduced by the additive and a more fragile ITZ.
- **R7 (Figure 13g):** Minimal visible surface cracking despite low strength, suggesting a more ductile, porosity-mediated deformation pathway in which energy is dissipated through distributed microcracking and matrix compaction rather than through large, well-defined macrocracks at the surface.

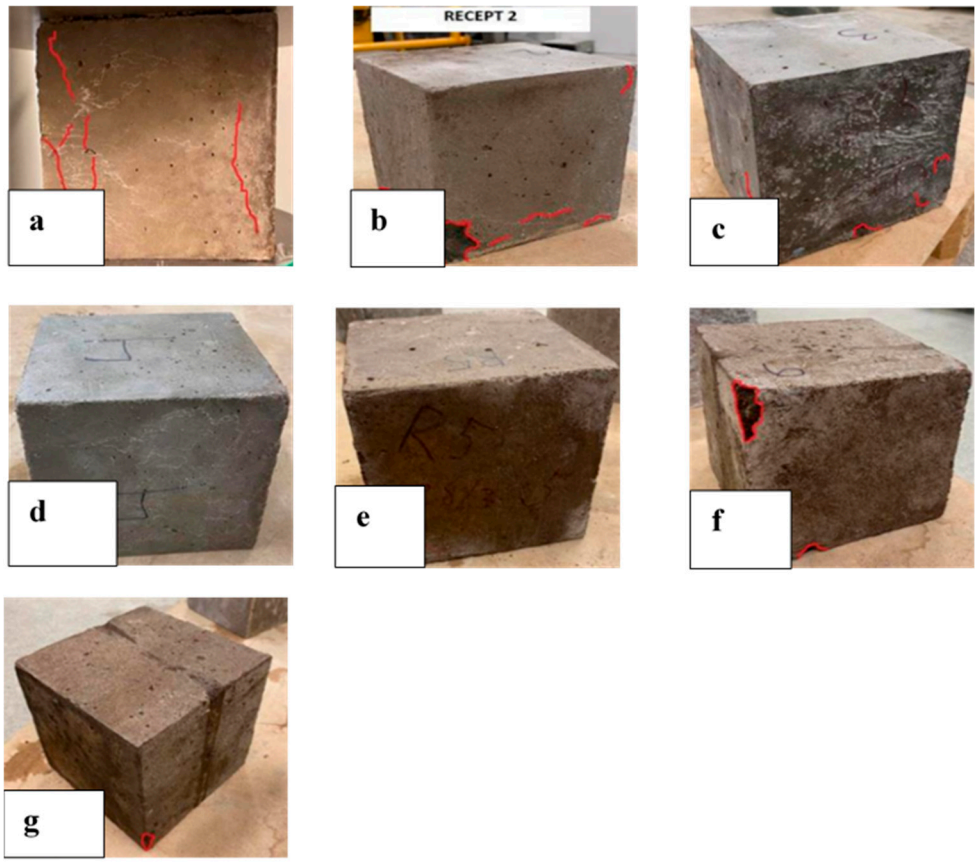

Figure 13. Visual documentation of pre-fire cracking for all recipes (R1–R7). (**a**) for R1, (**b**) for R2, (**c**) for R3, (**d**) for R4, (**e**) for R5, (**f**) for R6 and (**g**) for R7.

Taken together, the crack morphologies corroborate the strength hierarchy by revealing how each mix partitions damage between the paste, ITZ, and aggregate. Mixes with

greater early-age stiffness and stronger ITZ (e.g., R1) exhibit tight, evenly distributed microcracks, whereas systems with slower hydration or higher porosity (e.g., R2, R6, R7) show either localized spalling or subdued surface cracking consistent with diffuse internal damage. The fibre-modified slag blend (R4) illustrates the role of PP fibres in suppressing visible cracking without necessarily enhancing peak compressive strength. This distinction becomes important when assessing post-fire residual performance.

7.2. Heating Testing

Fire resistance was evaluated using a furnace protocol conforming to the ISO 834-time temperature curve [70], which reproduces the steep thermal ramp, ensuing thermal shock, and sustained high-temperature plateau characteristic of compartment fires. Specimens were heated to a peak of ≈950 °C to represent fully developed conditions. Both phenomenological responses (spalling, explosive splitting, surface cracking, and visible thermal expansion) and quantitative outcomes (mass loss and qualitative post-fire integrity) were recorded. Mass loss was computed as:

$$\text{Mass loss}(\%) = \frac{m_o - m_f}{m_o} \cdot 100 \quad (3)$$

where m_o and m_f Denote pre- and post-exposure masses, respectively. Observations for each mixture are provided in Figure 14a–g, and a consolidated summary is given in Figure 14 and Table 5. The cross-recipe trend in mass loss is synthesized in Figure 15 (line diagram) and discussed below.

Figure 14. (**a**–**g**) Visual documentation of post-fire cracking for all recipes (R1–R7).

Table 5. Mass loss after ISO 834-1 fire exposure for all recipes (R1–R7).

Recipe	Mass Loss [g]	Loss of Mass [%]
1	1527	19.2
2	1378.5	18.0
3	2595	33.0
4	688	8.84
5	1329	18.5
6	645	8.79
7	647.5	9.4

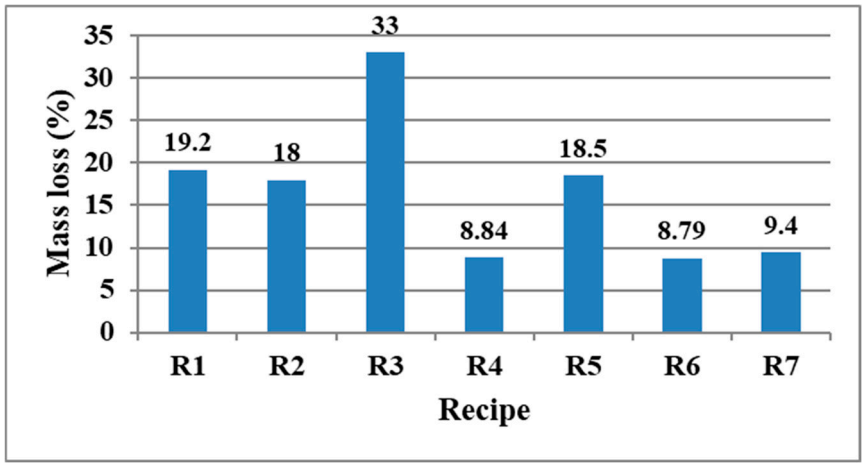

Figure 15. Mass loss after ISO 834-1 fire exposure for R1–R7.

Recipe 1 (R1) (100% Cement), underwent explosive spalling upon heating. One face remained largely intact while the others fragmented, with blocky pieces breaking from the edges and corners. This pattern, along with a mass loss of 19.2% (see Table 5), indicates a failure caused by trapped steam vapor pressure and stress concentration at the aggregate-paste interface. The dense, low-permeability matrix of this plain Portland cement concrete, which lacked fibers or pores to provide pressure relief, explains its severe spalling compared to modified mixes.

Recipe 2 (50% Cement, 50% Slag), (R2) experienced extensive surface spalling, especially on corners, with an 18.0% mass loss. Despite GGBFS improving long-term durability, it created a tight matrix at this testing age that trapped steam pressure, leading to failure similar to R1. High temperatures also weakened the slag-modified hydrates, making the matrix brittle. The refined porosity from slag was insufficient for pressure release during rapid heating, offering no spalling benefit.

Recipe 3 (90% Cement, 10% Biochar), (R3) showed the most severe damage, with catastrophic corner loss and deep erosion, resulting in the highest mass loss of 33.0%. This extreme spalling is due to biochar's highly porous and water-absorbent nature. Upon heating, the trapped moisture rapidly turns to steam, creating intense internal pressure, especially at corners. Biochar's low thermal conductivity and hydrophilic properties worsened the pressure build-up, leading to explosive failure dominated by pore pressure rather than gradual softening.

Recipe 4 (50% Slag + PP Fibre), (R4) resisted explosive spalling, developing only a network of thermal cracks while maintaining its overall shape. Its mass loss was low at 8.84%. This performance is due to the polypropylene fibres, which melt and create channels

that release internal steam pressure, preventing violent failure. The damage was thus structurally contained, demonstrating the efficacy of fibres in providing pressure relief and significantly improving spalling resistance.

Recipe 5 (95% Cement, 5% Hydrochar), R5 showed significant surface cracking but no explosive spalling, with a mass loss of 18.5%. The 5% hydrochar replacement likely introduced limited permeability and stress-absorbing zones, which helped vent some vapor pressure and prevented violent failure. However, this small dosage was insufficient to fully prevent major cracking. The similar mass loss to plain mixes suggests that low hydrochar content offers only partial mitigation and does not fundamentally alter the material's response under severe thermal stress.

Recipe 6 (90% Cement, 10% Hydrochar), (R6) exhibited no spalling, with only thermal cracking observed. The specimen expanded and softened during heating, resulting in minimal mass loss of 8.79%. This superior performance is attributed to the higher hydrochar content, which increased microporosity and provided effective vapor escape routes. The balance between permeability for pressure relief and matrix cohesion prevented explosive failure, indicating that the higher hydrochar fraction shifted the material beyond a critical threshold into a damage regime dominated by controlled cracking.

Recipe 7 (80% Cement, 20% Hydrochar), (R7) demonstrated superior fire resistance with no cracking or spalling, only thermal expansion, and a low mass loss of 9.4%. This performance is attributed to the high hydrochar content, which creates interconnected pores for vapor release and disrupts heat conduction, reducing internal pressure buildup. However, this enhanced fire tolerance coincided with the lowest pre-fire compressive strength, highlighting a key trade-off between fire resilience and ambient strength that requires balanced design considerations.

Cross-Recipe Synthesis and Implications, the mixes separate into two distinct groups based on fire performance. R4, R6, and R7 show low mass loss (8.8–9.4%) and non-explosive, crack-dominated failure. In contrast, R1–R3 and R5 exhibit higher mass loss and explosive spalling. The performance ranking (R7 $\approx$ R6 $\approx$ R4 $\gg$ R2 $\approx$ R5 $\approx$ R1 $\gg$ R3) directly correlates with each mix's capacity for steam venting during rapid heating. The results confirm that fire resistance depends primarily on creating connected pathways for steam release (via fibers or high hydrochar content), not on ambient density, though this often involves a trade-off with pre-fire compressive strength.

7.3. Compressive Strength Test After Fire

Figure 16a juxtaposes pre- and post-fire compressive strengths for R1–R7, providing a direct bridge between the baseline values in Figure 12 and the residual capacities measured after heating. Figure 16b presents the retained strength expressed as a percentage of pre-fire capacity, and Table 6 lists the corresponding reduction ratios. As illustrated, Recipe 3 exhibits the most significant reduction ($\approx$83.2%). In comparison, Recipe 7 shows the smallest ($\approx$66.6%), with the remaining mixes falling between these bounds in a pattern consistent with the mass-loss and damage groupings described in Section 7.

7.4. Cracking from Compression Test After Fire

Representative post-fire cracking observed after uniaxial compression is documented in Figure 17a–g. Following thermal exposure, the specimens predominantly failed by through-thickness splitting accompanied by spalling, with crack apertures sufficiently large to release sizable fragments from the core. In Recipe 1 (Figure 17a), the dominant feature was a wide, continuous fracture that traversed the section and precipitated the detachment of large pieces; a pronounced vertical crack was also evident along the right face. Recipe 2 (Figure 17b) exhibited a clear escalation in severity relative to Recipe 1, with

deeper and wider fractures, greater crack multiplicity, and more extensive material loss, indicating a more brittle post-fire response under compression. For Recipe 3 (Figure 17c), deep primary fractures were again present, but these were accompanied by finer, randomly oriented fissures that suggest additional microcrack coalescence beyond that seen in the earlier mixes.

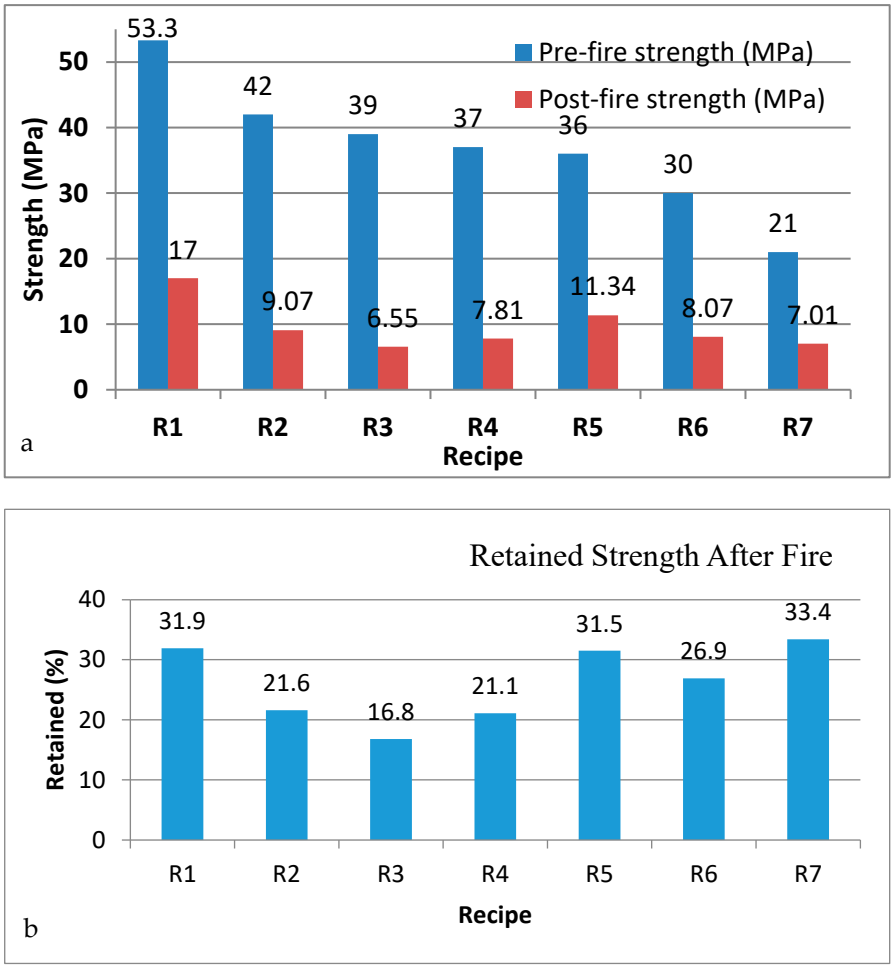

Figure 16. Post-fire compressive performance (line diagrams). (**a**) Pre- vs. post-fire compressive strength for R1–R7. (**b**) Retained strength after fire (% of pre-fire) for R1–R7.

Table 6. Reduction percentage in compression after fire.

	R1	R2	R3	R4	R5	R6	R7
Reduction	68.1	78.4	83.2	78.9	68.5	73.1	66.6

Recipe 4 (Figure 17d) exhibited a spatially distributed crack network that closely resembled that of Recipe 3, characterized by widely propagated, deep cracks that liberated large fragments from multiple faces. In Recipe 5 (Figure 17e), deep, wide fractures and associated spalling were still observable; however, the overall extent and dispersion of damage were comparatively lower, making this mix the least susceptible to cracking under the combined effects of fire and subsequent compression in the present series. Recipe 6 (Figure 17f) marked the upper bound of damage severity, with the highest observed crack density. Fractures were both deep and widely distributed, and large sections disengaged from the body, consistent with extensive loss of load-carrying integrity after heating. Finally, Recipe 7 (Figure 17g) mirrored the behavior of Recipes 5 and 6: long, well-distributed

fractures traversed the specimen, the entire cross-section displayed visible cracking, and sizeable chunks detached. Taken together, the qualitative ranking of crack severity increased from Recipe 1 to a peak at Recipe 6, with Recipe 5 demonstrating relative resistance, and Recipe 7 presenting a widely distributed, cross-section-spanning crack pattern comparable to the more damage-prone mixes.

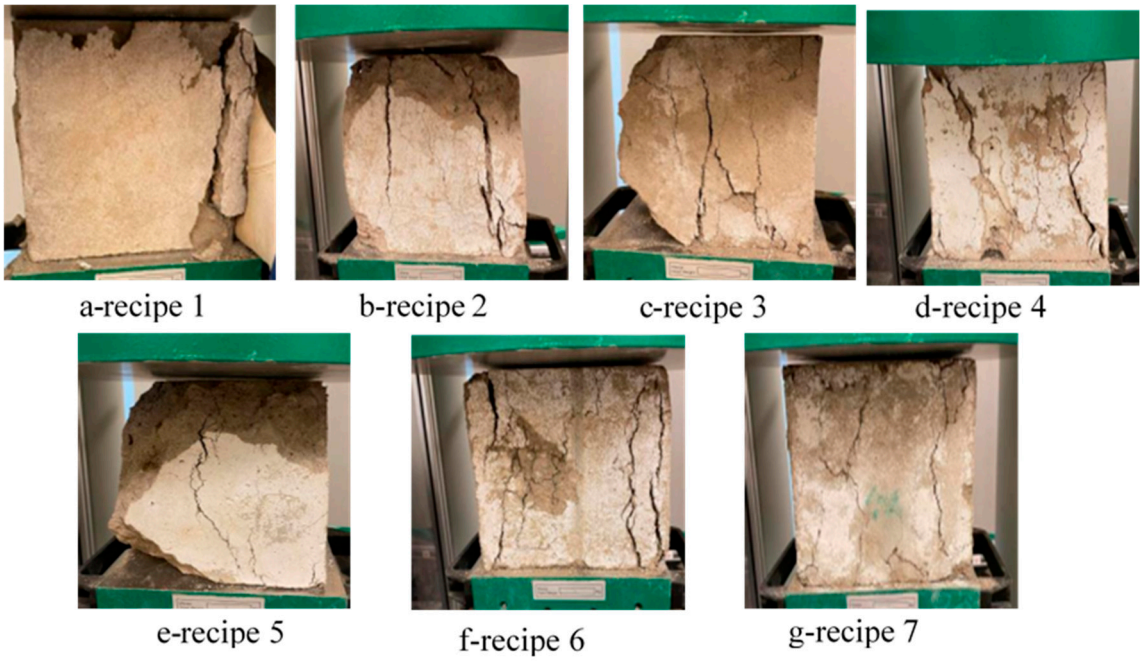

Figure 17. Cracks resulting from compression after fire exposure for each recipe.

7.5. In-Depth Analysis of Temperature Effects on Concrete Behavior

The thermochemical and mechanical degradation of concrete under elevated temperatures follows well-established mechanisms that provide critical context for interpreting the experimental results. As temperature rises, key transformations occur that directly explain the performance variations observed across mixes R1–R7.

Thermo-Chemical Degradation Progression:

100–300 °C: Evaporation of free water and initiation of C-S-H gel dehydration begins, leading to initial strength reduction and microcrack formation [54,61].

400–600 °C: Decomposition of Portlandite ($Ca(OH)_2$) occurs around 450 °C, releasing chemically bound water and creating additional porosity. Concurrently, advanced C-S-H degradation causes significant strength loss and increased permeability [51,61]. 700–900 °C: Complete decomposition of hydration products and quartz transformation in aggregates (α- to β-quartz at 573 °C) results in substantial mechanical deterioration and color changes observed in our specimens [54].

Thermo-Mechanical Damage Mechanisms:

The differential thermal expansion between aggregate (typically 6–12 $\times$ 10^{-6}/°C) and cement paste (approximately 18 $\times$ 10^{-6}/°C) generates internal stresses that initiate microcracking, particularly evident in the crack patterns of R1-R3 (Figures 13, 14 and 17). This thermal incompatibility is exacerbated in dense matrices like R1, where restrained expansion leads to tensile failure at the interfacial transition zone (ITZ).

Pore Pressure Development:

The rapid heating rate of the ISO 834-1 curve (reaching approximately 840 °C in 30 min) creates steep moisture gradients. In low-permeability mixes (R1, R2), vapor migration cannot keep up with steam production, leading to critical pore pressure buildup that

exceeds the tensile strength of the matrix—explaining the explosive spalling behavior. This phenomenon is well-documented in literature, where pressures can reach 2–8 MPa under similar conditions [12,68].

Additive-Specific Thermal Responses:

The superior performance of R4 (PP fibers) aligns with established pressure relief mechanisms, where fiber melting at approximately 165 °C creates interconnected void networks for vapor escape [15,58]. Similarly, hydrochar's effectiveness in R6–R7 can be attributed to its microporous structure providing pre-existing venting pathways, reducing the vapor pressure peaks that drive explosive spalling. These fundamental temperature-dependent processes provide the mechanistic foundation for understanding the comparative performance ranking (R7 ≈ R6 ≈ R4 ≫ R2 ≈ R5 ≈ R1 ≫ R3) and underscore the importance of engineered permeability in fire-resistant concrete design. The evidence across all recipes confirms three robust tendencies. First, partial clinker substitution—whether with GGBFS, biochar, or hydrochar—reduces baseline compressive strength at the tested age, with the extent depending on the degree of substitution and the reactivity of the additive. Second, fire exposure amplifies these differences by activating transport- and pressure-controlled degradation processes (moisture migration, vapor pressure buildup, and microcrack coalescence), which in turn influence spalling propensity and mass loss. Third, measures that reconfigure the pore network—either through engineered venting (PP fibers) or mesoporosity (higher hydrochar dosages)—reliably suppress explosive fragmentation but do not automatically guarantee better residual capacity; the latter depends on how much of the load-bearing hydrate skeleton survives the thermal cycle. These general patterns reconcile the mass-loss data (Figure 16), the absolute and normalized strength results (Figure 16a,b), and the additional cross-checks below. The purpose is to show how retained strength correlates with loss (calculated as 100 minus retained). R3 exhibits the largest reduction (about 83.2%), while R7 has the smallest (about 66.6%), defining the upper and lower bounds of proportional loss. This visualization highlights the trade-off between high initial capacity and vulnerability to thermal damage. Mixes with higher pre-fire MPa (e.g., R1) tend to experience larger proportional losses, whereas hydrochar-rich mixes (R6–R7) have lower initial capacity but smaller proportional losses.

7.5.1. Mix-Wise Interpretation in Light of Cross-Metric Trends

R1 (100% cement). The elevated pre-fire capacity results from a dense hydrate network with low capillary connectivity; however, the same permeability limitation causes vapor entrapment during the ISO 834-1 ramp. The resulting pressure transients appear macroscopically as explosive spalling (see Figure 14a), extensive material detachment (Figure 15), and a significant loss of residual capacity (Figure 16a,b). The post-fire compression response shows a through-section fracture with notable fragment release (Figure 17a). In the cross-metric view, R1 falls into the "high pre-fire MPa/high proportional reduction" quadrant of Figure 18, aligning with its position near the upper envelope of the figure.

R2 (50% slag). Replacing 50% of clinker with GGBFS reduces early-age strength compared to R1, consistent with the slower kinetics of slag hydration at the tested maturity [73]. Although the overall mass loss is slightly lower than in R1 (Figure 15), the proportional capacity loss is higher (Figure 18), indicating that the slag-bearing matrix remained vulnerable to thermally induced damage under rapid heating. The fracture pattern, characterized by shallow delaminations overlaid on corner loss (Figure 14b), and the more brittle response after fire (Figure 17b), suggest that the ITZ and matrix lacked sufficient pressure-relief pathways at higher temperatures. In Figure 19, R2 plots at intermediate pre-fire MPa levels still show a significant reduction, emphasizing the maturity sensitivity of slag systems at this age.

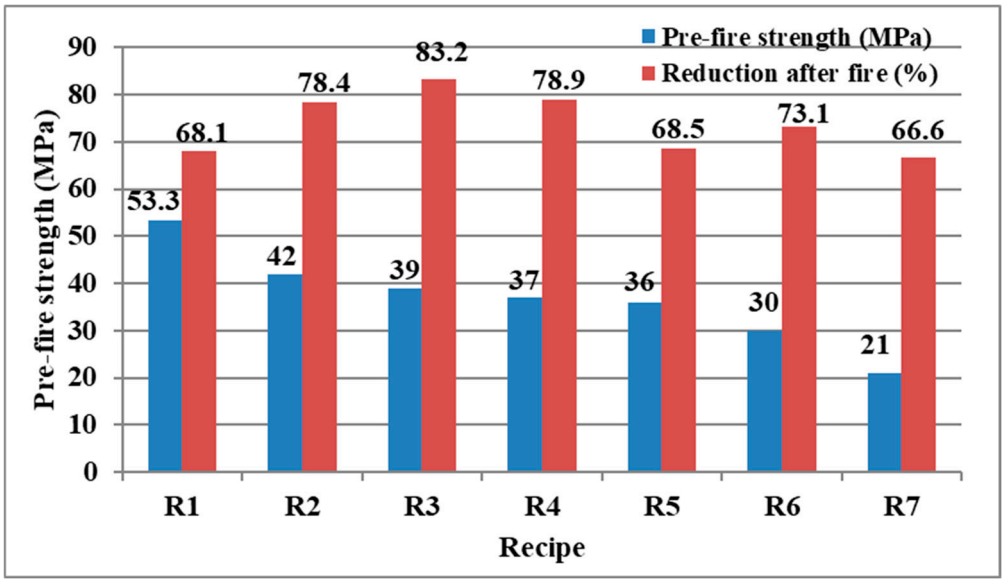

Figure 18. Pre-fire compressive strength versus reduction after fire for R1–R7 (dual-axis).

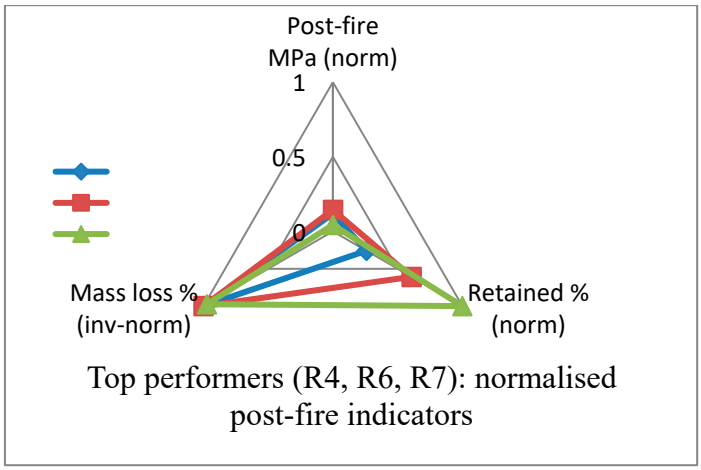

Figure 19. Radar chart of normalized post-fire indicators for R4, R6, R7.

R3 (90% cement, 10% biochar). Despite having acceptable pre-fire strength, R3 shows the worst fire-stage performance, marked by the highest mass loss (Figure 15), the largest proportional reduction (Figure 18), and severe corner and edge deterioration (Figure 14c). This outcome aligns with a microporous, water-retentive carbon phase that increases internal surface area and moisture storage; during rapid heating, this causes localized pore-pressure surges and erosive detachment, diverging from the benefits sometimes seen at lower biochar doses [11]. The post-fire compression pattern (Figure 17c), with deep primary fractures and fine, randomly oriented fissures, indicates widespread microcrack coalescence layered on top of dominant failure planes. In Figure 19, R3 is consistent with the high-reduction regime, even though it only had moderate pre-fire MPa.

R4 (50% slag + PP fibres). PP fibres reduce explosive spalling by melting to create temporary venting channels, as shown by the relatively low mass loss (Figure 15) and the lack of violent detachment in Figure 14d. However, the retained strength remains limited (Figure 16b), and the post-fire compression response displays a network of distributed cracks rather than catastrophic fragmentation (Figure 17d). This decoupling lessens fragmentation without a proportional preservation of load-bearing capacity, placing R4 at a moderate pre-fire MPa, but with a significant reduction, as indicated in Figure 19, and in the mid-range of Figure 18.

R5 (95% cement, 5% hydrochar). Even a small hydrochar fraction decreases the baseline capacity, but the mass-loss behavior remains close to R1–R2 (Figure 15). The proportional reduction occurs in the middle range (Figure 18), indicating that the pore-network modification is not enough to reach the threshold needed for significant pressure relief during the most intense heating phase. Morphologically, Figure 14e shows clear surface degradation without ejection, and Figure 17e confirms relatively limited cracking compared to the most damage-prone mixes. In Figure 19, R5 is at a lower pre-fire MPa with an intermediate reduction.

R6 (90% cement, 10% hydrochar). Increasing hydrochar seems to push the system past a permeability or compliance threshold: explosive spalling is not seen (Figure 14f), mass loss remains among the lowest (Figure 15), and the retained fraction improves (Figure 16b) despite the lower baseline MPa (Figure 16a). The post-fire compression pattern (Figure 17f) is characterized by controlled cracking rather than widespread detachment. Consequently, Figure 19 shows R6 at the lower MPa/lower reduction point, and Figure 18 verifies a reduction smaller than that of R1–R4.

R7 (80% cement, 20% hydrochar). The highest hydrochar replacement results in the smallest proportional loss (Figure 18) and low mass detachment (Figure 15), with minimal visible cracking during fire exposure (Figure 14g) and a widespread but non-catastrophic crack pattern under post-fire compression (Figure 17g). The trade-off is a lower absolute pre-fire capacity (Figure 16a); however, the retained fraction remains the best in the series (Figure 16b). In Figure 19, R7 represents the corner of "low pre-fire MPa/low proportional reduction," illustrating a robustness-focused design approach where microporosity and controlled gradients shift failure from explosive fragmentation to managed cracking. Overall, the analysis across Figures 15, 16a,b, 18, and 19 reveals two performance groups: (i) dense or maturity-limited systems (R1–R3, partly R5) with higher initial MPa but weaker thermal robustness, and (ii) vented/mesoporous systems (R4, R6, R7) that minimize fragmentation and, for hydrochar-rich mixes, reduce proportional loss—even if they compromise pre-fire strength.

7.5.2. Cross-Metric Implications for Testing and Design

Taken together, Figures 15, 16, 18 and 19 suggest two practical strategies for fire-resistant design. The first is engineered venting, exemplified by PP fibres (R4), which reliably prevents explosive failure and minimizes mass loss. The second involves tuning the pore network through hydrochar (R6–R7), which not only limits fragmentation but also reduces proportional strength loss in this dataset. Neither method alone guarantees high absolute residual strength: achieving that requires a baseline capacity sufficient to meet service demands after the expected percentage loss. Therefore, the design should focus on post-fire performance targets, combining (i) minimum pre-fire MPa, (ii) maximum allowable reduction (%), and (iii) acceptable damage mode (fragmentation vs. controlled cracking). When safety margins depend on residual capacity—such as in columns with limited redundancy—hybrid strategies that combine moderate hydrochar with low-dose fibres seem promising, provided curing and maturity are carefully controlled to prevent early-age deficits.

7.5.3. Robustness Checks and Sources of Uncertainty

Interpretation must recognize several constraints inherent to small-scale testing. Variability between specimens, local temperature gradients within the furnace, and moisture content fluctuations introduce noise into mass-loss and strength measurements. Additionally, some specimens (notably R1–R3 and R5) were subjected to post-fire compression in a damaged state due to splitting, which reflects real-world post-fire assessment but

diverges from ideal protocols that test intact cubes. The mass-loss metric combines material detachment with evaporated moisture, so low mass loss does not necessarily indicate high residual MPa unless considered alongside Figures 16a,b and 19. Finally, slag systems (R2, R4) are known to be sensitive to maturity; later ages or activation strategies may alter their position on the strength–robustness spectrum, requiring targeted follow-up.

8. Discussion

This study shows that residual performance after standard-fire exposure depends less on ambient-condition density and more on the availability, connectivity, and stability of vapour-relief pathways during the rapid ISO 834 heating phase. By examining Figures 15, 16a,b, 19 and 20, two typical behaviors become evident. The first is a strength-focused but thermally vulnerable regime, characterized by dense matrices with low intrinsic permeability (R1) and, at the tested maturity, slag systems without extra venting (R2). These mixes start with relatively high pre-fire capacity but experience significant mass loss and notable proportional strength reductions when heated. The second is a robustness-focused regime, shown by mixes with engineered venting (PP fibres, R4) or mesoporosity tuning (hydrochar, R6–R7). These reduce explosive spalling and mass loss, maintaining a larger portion of strength, although they begin with a lower baseline compressive capacity. The overall comparison, including the trade-off between fragmentation control and capacity retention, is summarized in the synthesis plots provided below. This contrast is visualized in Figure 20, which compares the top-performing mixes (R4, R6, R7) across normalized post-fire indicators.

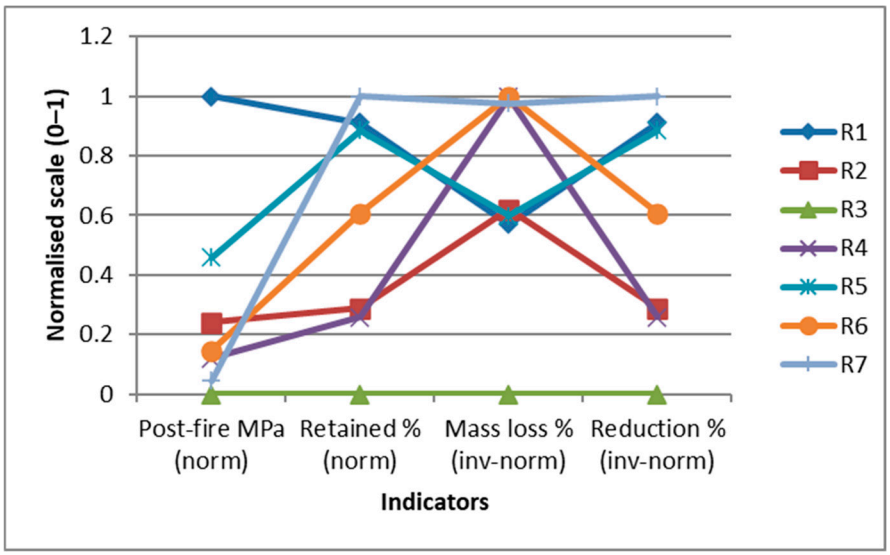

Figure 20. Parallel-coordinates plot of normalized indicators for R1–R7 (post-fire MPa, retained %, inverted mass loss %, inverted reduction %).

8.1. Mechanistic Interpretation

The observed transitions under the standard fire curve are consistent with a coupled transport–thermo-mechanical framework. In dense matrices at low water-cement ratios, vapor generation outpaces through-thickness migration, building pore-pressure transients that act in tandem with thermal expansion mismatch at the paste–aggregate interface. Microcracks nucleate preferentially at defects and interfacial transition zones, coalesce along planes of maximum tensile stress, and culminate in fragmentation where pressure release is abrupt. The macro-scale signatures, as indicated by the upper-envelope reductions

in Figure 18, the higher mass losses in Figure 15, and the post-fire crack patterns observed in Figure 17, align with this picture.

Two mitigation strategies explain the second archetype. First, polypropylene fibers (R4) melt early in the thermal cycle, generating a distributed network of transient capillaries. These pathways accommodate vapor flow and depress internal pressure peaks, converting explosive spalling into non-violent, through-section cracking. The result is a significantly lower mass loss, accompanied by only moderate gains in retained capacity (compare Figures 15 and 16b), which highlights the difference between surface integrity and load-bearing capacity. Second, hydrochar additions (R6–R7) pre-configure a mesoporous network that increases vapor connectivity and reduces local thermal gradients. This shifts failure towards controlled cracking and systematically reduces proportional loss (see Figures 19 and 20). The downside is a lower baseline MPa (Figure 16a), reflecting clinker dilution and modified hydration kinetics; however, the retained capacity improves, which is crucial when design is governed by residual capacity rather than peak ambient strength.

The outlying response of R3 (10% biochar), with the most significant mass loss and proportional reduction, underscores the sensitivity of carbonaceous additions to pore-scale moisture interactions and fineness. Microporous, water-retentive domains can delay venting and intensify local pressure surges, thereby promoting corner losses and the formation of deep erosive channels. The divergence between low-dose benefits sometimes reported elsewhere and the present outcome at 10% is plausibly explained by dosage and processing, consistent with the degraded placement of R3 across Figures 15 and 19 without contradicting the broader framework established here.

8.2. Trade-Offs and Design Envelopes

The cross-metric plots (Figures 19 and 20) articulate a central design tension. Mixes with higher pre-fire MPa tend, in this dataset, to experience greater proportional losses under rapid heating. In contrast, systems engineered for venting or mesoporosity retain a larger strength fraction but start from lower baselines. Consequently, specification is best framed as a performance envelope comprising three coupled targets:

i. A minimum pre-fire compressive strength to meet serviceability and design actions;
ii. A maximum allowable reduction (or, equivalently, a minimum retained fraction) after standard-fire exposure;
iii. An admissible damage mode, in which explosive fragmentation is prohibited and controlled cracking is acceptable.

Within such envelopes, multiple solutions are admissible. Where cover integrity and spalling control are paramount, e.g., to protect reinforcement continuity or limit debris, an R4-type route (slag + PP fibres) is compelling: mass loss is minimized and detachment is avoided, even if the retained MPa is only moderate. Where post-fire residual capacity is the governing limit state, hydrochar-rich solutions (R6–R7) may be preferred: despite lower baseline MPa, they deliver smaller proportional reductions and a more forgiving failure mode. Combining a moderate hydrochar dosage with a modest fibre content is a pragmatic approach to moving mixes closer to the desired envelope corner, provided that curing and maturity are controlled.

To generalise beyond the top three, Figure 20 provides a parallel-coordinates comparison of all mixes (R1–R7) across normalised indicators, making recipe-specific trade-offs explicit and enabling rapid screening against envelope targets.

8.3. Practical Implications

Three practice-oriented points follow. First, visual integrity does not indicate the actual capacity retention. While suppressing explosive spalling improves inspectabil-

ity and limits debris, structural safety must be evaluated based on post-fire MPa and retained fraction (cf. Figures 16a,b and 19). Second, hydrochar dosage acts as a tunable factor for robustness: increasing its content within the current range shifts the failure mode from fragmentation to controlled cracking and decreases proportional loss (Figures 19 and 20), but it also lowers pre-fire capacity (Figure 16a); therefore, dosage should be selected according to the needed residual MPa. Third, controlling maturity and curing is essential for slag systems; at the tested age, the pore network stayed relatively tight, and the thermal shock response did not resemble that of the control unless fibers were included. Adjusting curing or activation can move slag blends toward greater robustness without sacrificing sustainability goals. Additionally, quality-control measures should reflect these dual objectives. Pre-qualification may include retained-strength testing under a standard fire curve, reporting both the absolute residual strength in MPa and the percentage reduction, along with a documented damage mode (fragmentation vs. controlled cracking). Routine production checks should monitor moisture content at testing, as small variations in internal moisture can significantly influence pore-pressure histories and therefore apparent robustness.

8.4. Limitations and Uncertainty

Typical constraints of small-scale furnace testing limit interpretation. Variability between specimens, local thermal gradients, and differences in moisture content introduce scatter in mass loss and strength measurements. The mass-loss measure combines material detachment with evaporated moisture; therefore, a low percentage does not necessarily indicate high residual capacity unless supported by Figures 16a,b and 19. Some specimens (e.g., R1–R3, R5) were compressed while already in a pre-damaged state due to splitting, which reflects a realistic post-fire condition but is conservative compared to tests on intact cubes. Carbonaceous additives are also sensitive to processing parameters: particle size distribution, surface chemistry, and ash content affect hydration kinetics, pore structure, and water retention, thus influencing the observed response. Lastly, size and restraint effects that are insignificant in small cubes may become significant in larger members, where thermal gradients, boundary conditions, and reinforcement restraint lead to different cracking behaviors.

9. Conclusions and Recommendations

This study shows that post-fire residual capacity cannot be accurately predicted from pre-fire strength. The following combined conclusions and useful recommendations are derived from the main findings.

Key Findings

Performance After a Fire Is Unpredictable Based on Initial Strength: After thermal loading, there was a notable change in the mixes' performance ranking. Even though some mixes with a high biochar content (like Recipe 3) had respectable pre-fire strength, their proportional strength loss was the most severe (≈83.2%). This suggests that thermal degradation may be more likely to occur in a microstructure optimized for ambient strength. While preventing explosive spalling during a fire is essential, splitting resistance is insufficient to ensure sufficient residual load-bearing capacity. Recipe 4 produced the highest residual compressive strength (7.8 MPa) and satisfied the splitting resistance requirement, making it the most balanced of the compliant mixes.

Strength Retention and Mass Loss Are Unrelated: Although mixes containing hydrochar demonstrated better resistance to mass loss (Recipes 5–7), this did not always result in high residual strength. This discrepancy demonstrates that mechanical performance must be evaluated directly and cannot be deduced from surface condition or mass loss

alone. There is a trade-off between performance metrics: Mixes high in hydrochar, notably Recipe 7, displayed the least amount of mass loss and the smallest proportionate strength decline (≈66.6%). However, their low baseline strength may limit their application when a high absolute post-fire capacity is required.

Author Contributions: Conceptualization, A.A. and M.A.-G.; Methodology, Software, Validation, A.V.; Formal Analysis, M.A.-G.; Data Curation, A.A.; Writing—Original Draft Preparation, A.A.; Writing—Review & Editing, A.M. and A.V.; Visualization, A.A. and M.A.-G.; Supervision, Project Administration, A.A. All authors have read and agreed to the published version of the manuscript.

Funding: This research received no external funding.

Institutional Review Board Statement: Not applicable.

Informed Consent Statement: Not applicable.

Data Availability Statement: The original contributions presented in the study are included in the article, further inquiries can be directed to the corresponding author.

Conflicts of Interest: The authors declare no conflict of interest.

Abbreviations

Abbreviation	Full Term
PP	Polypropylene
GGBFS	Ground-Granulated Blast-Furnace Slag
SCM	Supplementary Cementitious Material
w/c	Water-to-Cement Ratio
ITZ	Interfacial Transition Zone
C–S–H	Calcium-Silicate-Hydrate
R1–R7	Recipe 1 to Recipe 7
CO_2	Carbon Dioxide
LCA	Life Cycle Assessment
CCUS	Carbon Capture, Utilization, and Storage
SEM	Scanning Electron Microscope
ISO	International Organization for Standardization
EN	European Norm
ASTM	American Society for Testing and Materials
BBR	Boverket's Building Regulations
TGA/DSC	Thermogravimetric Analysis/Differential Scanning Calorimetry

References

1. Almssad, A. *Betongkonstruktion*, 3rd ed.; Studentlitteratur: Lund, Sweden, 2022.
2. GCCA. *Concrete Future Roadmap*; Global Cement and Concrete Association: London, UK, 2021. Available online: https://gccassociation.org/concretefuture/ (accessed on 15 March 2025).
3. Samad, S.; Shah, A. Role of binary cement including Supplementary Cementitious Material (SCM), in production of environmentally sustainable concrete: A critical review. *Int. J. Sustain. Built Environ.* **2017**, *6*, 663–674. [CrossRef]
4. Kazemi, N. Reasons for crack propagation and strength loss in refractory castables based on changes in their chemical compositions and micromorphologies with heating: Special focus on the large blocks. *J. Asian Ceram. Soc.* **2019**, *7*, 109–126. [CrossRef]
5. Luhar, S.; Nicolaides, D.; Luhar, I. Fire resistance behaviour of geopolymer concrete: An overview. *Buildings* **2021**, *11*, 82. [CrossRef]
6. Xie, A.; Wu, W.; Zhou, Q. Biochar as a sustainable additive in fired clay bricks and building blocks: Processing, properties, and performance. *Constr. Build. Mater.* 2025, *in press*. [CrossRef]
7. Kodur, V.; Kumar, P.; Rafi, M.M. Fire hazard in buildings: Review, assessment and strategies for improving fire safety. *PSU Res. Rev.* **2020**, *4*, 1–23. [CrossRef]
8. Zhang, Z.; Li, Z.; He, J.; Qian, S.; Shi, X. Recycled mask polypropylene microfibers benefit tensile properties and prevent thermally induced spalling of high-strength engineered cementitious composite (HS-ECC). *J. Clean. Prod.* **2024**, *457*, 142476. [CrossRef]

9. Brennan, M.C.; Keist, J.S.; Palmer, T.A. Defects in Metal Additive Manufacturing Processes. *J. Mater. Eng. Perform.* **2021**, *30*, 4808–4818. [CrossRef]
10. Khoury, G.A. Effect of fire on concrete and concrete structures. *Prog. Struct. Eng. Mater.* **2000**, *2*, 429–447. [CrossRef]
11. La Scala, A.; Carnimeo, L. Effective Comparison of Thermo-Mechanical Characteristics of Self-Compacting Concretes Through Machine Learning-Based Predictions. *Fire* **2025**, *8*, 289. [CrossRef]
12. *EN 13501-1:2018*; Fire classification of construction products and building elements—Part 1: Classification using data from reaction to fire tests. European Committee for Standardization: Brussels, Belgium, 2018.
13. Millard, A.; Pimienta, P. *Modelling of Concrete Behaviour at High Temperature*; Springer International Publishing: Cham, Switzerland, 2019. [CrossRef]
14. Li, Y. Material Properties and Explosive Spalling of Ultra-High Performance Concrete in Fire. Ph.D. Thesis, Nanyang Technological University, Singapore, 2018.
15. Hager, I.; Mróz, K. Role of polypropylene fibres in concrete spalling risk mitigation in fire and test methods of fibres effectiveness evaluation. *Materials* **2019**, *12*, 3869. [CrossRef]
16. *EN 206:2020*; Concrete—Specification, Performance, Production and Con-Formity. European Committee for Standardization: Brussels, Belgium, 2020.
17. Beaudoin, J.; Odler, I. Hydration, setting and hardening. In *Lea's Chemistry of Cement and Concrete*, 5th ed.; Hewlett, P., Liska, M., Eds.; Butterworth-Heinemann: Oxford, UK, 2019; pp. 157–200.
18. Bahurudeen, A.; Dhanya, B.; Santhanam, M. Concrete as an artificial rock: Mineralogy of aggregates revisited. *Indian Concr. J.* **2022**, *96*, 5–36.
19. Kondraivendhan, B.; Bhattacharjee, B. Strength and w/c ratio relationship of cement based materials through pore features. *Mater. Charact.* **2016**, *122*, 124–129. [CrossRef]
20. Habert, G.; Miller, S.A.; John, V.M.; Provis, J.L.; Favier, A.; Horvath, A.; Scrivener, K.L. Environmental impacts and decarbonization strategies in the cement and concrete industries. *Nat. Rev. Earth Environ.* **2020**, *1*, 559–573. [CrossRef]
21. Majid Al-Gburi, M.; Gonzalez-Libreros, J.; Sas, G.; Nilsson, M. Quantifying Environmental Impacts of Railway bridge Using Life Cycle Assessment: A Case Study. In Proceedings of the IABSE Symposium Prague, "Challenges for Existing and Oncoming Structures", Prague, Czech Republic, 25–27 May 2022; pp. 1796–1803.
22. Madlool, N.; Saidur, R.; Rahim, N.; Kamalisarvestani, M. An overview of energy savings measures for cement industries. *Renew. Sustain. Energy Rev.* **2013**, *19*, 18–29. [CrossRef]
23. Favier, A.; Scrivener, K.; Habert, G. Decarbonizing the cement and concrete sector: Integration of the full value chain to reach net zero emissions in Europe. In *IOP Conference Series: Earth and Environmental Science*; IOP Publishing: Bristol, UK, 2019; Volume 225, p. 012009.
24. Chatterjee, A.; Sui, T. Alternative fuels—Effects on clinker process and properties. *Cem. Concr. Res.* **2019**, *123*, 105777. [CrossRef]
25. Juenger, M.C.G.; Siddique, R. Recent advances in understanding the role of supplementary cementitious materials in concrete. *Cem. Concr. Res.* **2015**, *78*, 71–80. [CrossRef]
26. Slunge, D.; Miguel, M.; Lindahl, L.; Backhaus, T. The implementation of the substitution principle in European chemical legislation: A comparative analysis. *Environ. Sci. Eur.* **2023**, *35*, 107. [CrossRef]
27. Paltsev, S.; Morris, J.; Kheshgi, H.; Herzog, H. Hard-to-Abate Sectors: The role of industrial carbon capture and storage (CCS) in emission mitigation. *Appl. Energy* **2021**, *300*, 117322. [CrossRef]
28. Schumacher, K.; Chu, P.; Platt, S.; Newman, A.; Garboczi, E.; Beers, K.L. *Fostering a Circular Economy and Carbon Se-questration for Construction Materials Workshop Report: A Focus on Concrete*; National Institute of Standards and Technology: Gaithersburg, MD, USA, 2023.
29. Al-Gburi, M.; Abed, J.; Almssad, A.; Alhayani, A.A.; Jędrzejewska, A.; Nilsson, M. The effect of real curing temperatures on early age concrete strength development in massive concrete structures. *Eur. J. Environ. Civ. Eng.* **2025**, *29*, 1832–1847. [CrossRef]
30. Felekoglu, B.; Tosun-Felekoglu, K.; Ranade, R.; Zhang, Q.; Li, V.C. Influence of matrix flowability, fiber mixing procedure, and curing conditions on the mechanical performance of HTPP-ECC. *Compos. Part B Eng.* **2014**, *60*, 359–370. [CrossRef]
31. Nematollahzade, M.; Tajadini, A.; Afshoon, I.; Aslani, F. Influence of different curing conditions and water to cement ratio on properties of self-compacting concretes. *Constr. Build. Mater.* **2020**, *237*, 117570. [CrossRef]
32. Lothenbach, B.; Winnefeld, F. Thermodynamic modelling of the hydration of Portland cement. *Cem. Concr. Res.* **2006**, *36*, 209–226. [CrossRef]
33. Ghebrab, T.T.; Soroushian, P. Mechanical properties of hydrated cement paste: Development of structure-property rela-tionships. *Int. J. Concr. Struct. Mater.* **2010**, *4*, 37–43. [CrossRef]
34. Long, Z.; Long, G.; Tang, Z.; Shangguan, M.; Zhang, Y.; Wang, L.; Yi, M. Hydration, strength, and microstructure evolution of Portland cement-calcium sulphoaluminate cement-CSH seeds ultra-early strength cementitious system. *Constr. Build. Mater.* **2024**, *430*, 136492. [CrossRef]

35. Jin, L.; Wang, Z.; Jiao, P.; Zhou, P.; Wu, T. Mesoscale-based failure mechanism of recycled aggregate concrete under axial compression considering end restraint effect. *Mater. Today Commun.* **2024**, *40*, 109549. [CrossRef]
36. Ambroziak, A.; Ziolkowski, P. Concrete compressive strength under changing environmental conditions during place-ment processes. *Materials* **2020**, *13*, 4577. [CrossRef]
37. Haavisto, J.; Husso, A.; Laaksonen, A. Compressive strength of core specimens drilled from concrete test cylinders. *Struct. Concr.* **2021**, *22*, E683–E695. [CrossRef]
38. *SS-EN 12390-1:2019*; Testing Hardened Concrete—Part 1: Shape, Dimensions and Other Requirements for Specimens and Moulds. Swedish Institute for Standards: Stockholm, Sweden, 2019.
39. *SS-EN 12390-2:2019*; Testing Hardened Concrete—Part 2: Making and Curing Specimens for Strength Tests. Swedish Institute for Standards: Stockholm, Sweden, 2019.
40. *SS-EN 12390-3:2019*; Testing Hardened Concrete—Part 3: Compressive Strength of Test Specimens. Swedish Institute for Standards: Stockholm, Sweden, 2019.
41. *SS-EN 12390-4:2019*; Testing Hardened Concrete—Part 4: Compressive Strength—Specification for Testing Machines. Swedish Institute for Standards: Stockholm, Sweden, 2019.
42. Al-Gburi, M.; Yusuf, S.A. Investigate the effect of mineral additives on concrete strength using ANN. *Asian J. Civ. Eng.* **2022**, *23*, 405–414. [CrossRef]
43. Li, Y.; Zhang, H.; Huang, M.; Yin, H.; Jiang, K.; Xiao, K.; Tang, S. Influence of different alkali sulfates on the shrinkage, hydration, pore structure, fractal dimension and microstructure of low-heat Portland cement, medium-heat Portland cement and ordinary portland cement. *Fractal Fract.* **2021**, *5*, 79. [CrossRef]
44. Hossain, M.M.; Karim, M.R.; Hasan, M.; Hossain, M.K.; Zain, M.F.M. Durability of mortar and concrete made up of pozzolans as a partial replacement of cement: A review. *Constr. Build. Mater.* **2016**, *116*, 128–140. [CrossRef]
45. Robayo-Salazar, R.; Muñoz, Y.; Erazo, K.; de Gutiérrez, R.M. Slurry infiltrated fiber concrete (SIFCON) for use in ballistic and fire protection of military structures. *Structures* **2023**, *57*, 105282. [CrossRef]
46. Wang, J.; Dai, Q.; Si, R.; Guo, S. Mechanical, durability, and microstructural properties of macro synthetic polypropylene (PP) fiber-reinforced rubber concrete. *J. Clean. Prod.* **2019**, *234*, 1351–1364. [CrossRef]
47. Wang, Y.; Zheng, K.; Yang, L.; Li, H.; Liu, Y.; Xie, N.; Zhou, G. Alkali-Activated Materials Reinforced via Fibrous Biochar: Modification Mechanisms, Environmental Benefits, and Challenges. *J. Compos. Sci.* **2025**, *9*, 298. [CrossRef]
48. Saha, N.; McGaughy, K.; Reza, M.T. Elucidating hydrochar morphology and oxygen functionality change with hydrothermal treatment temperature ranging from subcritical to supercritical conditions. *J. Anal. Appl. Pyrolysis* **2020**, *152*, 104965. [CrossRef]
49. Lahouar, M.A.; Pinoteau, N.; Caron, J.-F.; Foret, G.; Rivillon, P. Fire design of post-installed bonded rebars: Full-scale validation test on a 2.94 × 2 × 0.15 m3 concrete slab subjected to ISO 834-1 fire. *Eng. Struct.* **2018**, *174*, 81–94. [CrossRef]
50. Ariyanayagam, A.; Mahendran, M. Fire safety of buildings based on realistic fire time-temperature curves. In Proceedings of the 19th International CIB World Building Congress, Brisbane, Australia, 5–9 May 2013.
51. Byström, A.; Wickström, U. Temperature of post-flashover compartment fires—Calculations and validation. *Fire Mater.* **2018**, *42*, 255–265. [CrossRef]
52. Zentner, S. The Impact of Energy-and Building Policy on Property Companies in Sweden: Mandatory Regulations vs. Voluntary Commitments. Bachelor's Thesis, KTH Royal Institute of Technology, Stockholm, Sweden, 2017.
53. Wan, H.; Yu, L.; Ji, J. Experimental study on vertical temperature distribution of symmetry axis of two identical rectangular pool fires with long sides parallel. *Fire Saf. J.* **2021**, *120*, 103044. [CrossRef]
54. Pulkit, U.; Adhikary, S.D. Effect of micro-structural changes on concrete properties at elevated temperature: Current knowledge and outlook. *Struct. Concr.* **2022**, *23*, 1995–2014. [CrossRef]
55. Zhang, Q. Microstructure and Deterioration Mechanisms of Portland Cement Paste at Elevated Temperature. Ph.D. Thesis, Delft University of Technology, Delft, The Netherlands, 2013.
56. Muthanna Abbu, A.; Al-Attar, A.A.; Abd Alrahman, S.; Al-Gburi, M. The Mechanical Properties of Lightweight (Volcanic Pumice) Concrete Containing Fibers with Exposure to High Temperatures. *J. Mech. Behav. Mater.* **2022**, *31*, 812–823. [CrossRef]
57. Jhatial, A.A.; Goh, W.I.; Sohu, S.; Mohamad, N. Thermo-mechanical properties of various densities of foamed concrete incorporating polypropylene fibres. *Arab. J. Sci. Eng.* **2020**, *45*, 8171–8186. [CrossRef]
58. Boakye, K.; Khorami, M. Performance of Calcined Impure Kaolinitic Clay as a Partial Substitute for Portland Cement Concrete: A Review. *J. Compos. Sci.* **2025**, *9*, 145. [CrossRef]
59. Correia, J.; Lima, J.; de Brito, J. Post-fire mechanical performance of concrete made with selected plastic waste aggregates. *Cem. Concr. Compos.* **2014**, *53*, 187–199. [CrossRef]
60. RISE Research Institutes of Sweden. Quality Assurance of Concrete Elements for Reuse. Available online: https://www.ri.se/en/expertise-areas/services/quality-assurance-of-concrete-elements-for-reuse (accessed on 25 November 2024).
61. Kallimani, R.; Minde, P. Investigation on combined use of biochar and ground granulated blast furnace slag as a supplementary admixture in concrete. *Environ. Sci. Pollut. Res.* **2025**, *32*, 8201–8218. [CrossRef]

62. Liu, Q.; Tang, H.; Chen, K.; Sun, C.; Li, W.; Jiao, S.; Tam, V.W. Improving industrial drying process of recycled fine aggregates as a means of carbonation to improve the mechanical properties and plastic shrinkage of self-leveling mortar. *Constr. Build. Mater.* **2023**, *403*, 133001. [CrossRef]
63. Sioulas, B.; Sanjayan, J. The coloration phenomenon associated with slag blended cements. *Cem. Concr. Res.* **2001**, *31*, 313–320. [CrossRef]
64. Davies, G. Development of Sustainable Processes via Novel Synthesis Methods and Environments. Ph.D. Thesis, University of Sheffield, Sheffield, UK, 2021.
65. Asmadia, M.I.A.; Ismaila, R.; Zakwana, F.A.A.; Rashidb, R.S.M.; Zulkiflic, S.N.I. Structural Performance of Cellular Stainless-Steel Beams with Varied Web Hole Diameters Under Fire Conditions: Finite Element Analysis and Experimental Insights. *J. Kejuruter.* **2025**, *37*, 821–834. [CrossRef]
66. Charlier, M. Advanced Modelling of Travelling Fire for Structural Design: Experimental, Numerical and Analytical Investigations. Ph.D. Thesis, Ulster University, Belfast, UK, 2022.
67. Cardenas, N. Feasibility Study into the Use of Digital Image Correlation for Creep Strain Monitoring of Fossil Power Plant Welds. Master's Thesis, University of Bristol, Bristol, UK, 2018.
68. Boström, L. *Development of Test Methodology for Determination of Fire Spalling*; LUTVDG/TVBB; Report 1026; Lund University: Lund, Sweden, 2004; Volume 1026.
69. Bougara, A.; Lynsdale, C.; Milestone, N.B. The influence of slag properties, mix parameters and curing temperature on hydration and strength development of slag/cement blends. *Constr. Build. Mater.* **2018**, *187*, 339–347. [CrossRef]
70. Chaturvedi, S.; Vedrtnam, A.; Youssef, M.A.; Palou, M.T.; Barluenga, G.; Kalauni, K. Fire-resistance testing procedures for construction elements—A Review. *Fire* **2022**, *6*, 5. [CrossRef]
71. Gupta, S. Biochar Enhanced Concrete for Better Performance and More Effective Bio-Based Self Healing. Ph.D. Thesis, National University of Singapore, Singapore, 2018.
72. Khoury, G.A. Polypropylene fibres in heated concrete. Part 2: Pressure relief mechanisms and modelling criteria. *Mag. Concr. Res.* **2008**, *60*, 189–204. [CrossRef]
73. Özbay, E.; Erdemir, M.; Durmuş, H.İ. Utilization and efficiency of ground granulated blast furnace slag on concrete properties—A review. *Constr. Build. Mater.* **2016**, *105*, 423–434. [CrossRef]